Corrosion Science 257 (2025) 113319

Contents lists available at ScienceDirect

Corrosion Science

journal homepage: www.elsevier.com/locate/corsci

Assessment of carbon steel and corrosion resistant alloy corrosion in geothermal environments containing sulphuric acid

Joseph Thevakumar [a], Joshua Owen [a], Kathleen Purnell [a], Evgeny Barmatov [b], Richard Barker [a,*]

[a] Institute of Functional Surfaces, School of Mechanical Engineering, University of Leeds, Leeds LS2 9JT, United Kingdom
[b] Schlumberger Cambridge Research, High Cross, Madingley Road, Cambridge CB3 0EL, United Kingdom

ARTICLE INFO

Keywords:
Electrochemistry
Carbon steel
Stainless steel
Duplex steel
Geothermal
Sulphuric acid

ABSTRACT

This work focusses on understanding corrosion severity and pipeline material performance within model geothermal sulphuric acid (H_2SO_4)-containing environments. A tantalum-lined high pressure/high temperature autoclave is used to assess the corrosion behaviour of N80 carbon steel compared to 13 Cr and 22 Cr duplex stainless steel when exposed to H_2SO_4 solutions between a pH of 2–4, and at a temperature of 150 °C. Significant increases in solution pH were observed during 20-hour exposure experiments, resulting from acid consumption due to ongoing corrosion reactions. The resulting pH shift led to a notable reduction in corrosion rates over time, creating uncertainty when assessing long-term material degradation under variable environmental conditions. To address this uncertainty, corrosion rates were analysed in the early stages of exposures, enabling a reliable correlation between temperature, pH and metal composition. Linear polarisation resistance (LPR) measurements revealed that corrosion of carbon steel was primarily influenced by solution acidity, with temperature playing a secondary role. A comparative analysis of corrosion performance revealed that uniform and pitting corrosion rates decreased in the following order: carbon steel > 13 Cr stainless steel > 22 Cr duplex stainless steel. These results offer valuable insights into material selection and corrosion mechanisms relevant to geothermal energy applications.

1. Introduction

Renewable energy systems have gathered growing interest within many engineering sectors to encourage greener energy generation. The use of geothermal resources contributes to the global scope of minimising environmental pollution and utilising the constant availability of the Earth's natural heat. Extensive research indicates that a variety of geothermal systems are available over a range of operating temperatures and water chemistries [1–4]. While operating under different conditions, the well equipment associated with geothermal systems can experience corrosion and progressively lose functionality [5–8]. Materials performance at elevated temperatures and high-pH (pH > 4) geothermal environments is well understood [9–13], but knowledge of material behaviour at low-pH (pH < 4) geothermal environments containing sulphuric acid (H_2SO_4) is limited.

Generally, geothermal waters are found in underground reservoirs under the ground and between rocks that are naturally present due to specific geologies. Geothermal fluids primarily originate from meteoric or seawater sources, often mixed with some containing significant amounts of igneous volatiles. As volcanic gases are released from the Earth's core, the interaction between the underground water, rocks and gases can result in low pH geothermal waters. Nogara and Zarrouk summarised the main geological conditions responsible for the occurrence of acidic fluids in geothermal systems [14]. The most common source of acidity in operating geothermal wells worldwide is related to hydrogen chloride (Cl-type) and sulphuric acid type (SO_4-type) mainly known as "ultra-acidic brines" [15]. The combined acid sulphate-chloride (SO_4-Cl type) reservoir fluids, another common acid component, are commonly observed in arc-type geothermal systems along the circum-Pacific rim (in the Philippines, Japan, Taiwan, Indonesia, Costa Rica and Mexico [16–18]. At 25 °C, the pH of flashed acid SO_4-Cl water collected at the wellhead can be as low as 2. The most important difference between the Cl-type and SO_4-Cl type waters is that the main pH buffer of the former is CO_2/HCO_3^-, but HSO_4^-/SO_4^{2-} in the

* Corresponding author.
E-mail address: r.j.barker@leeds.ac.uk (R. Barker).

https://doi.org/10.1016/j.corsci.2025.113319
Received 17 July 2025; Received in revised form 13 September 2025; Accepted 13 September 2025
Available online 15 September 2025

Table 1
Concentrations of ions present in 1 L of geothermal brine solution.

Ion	ppm
Ca^{2+}	200
Mg^{2+}	347
K^{+}	1407
Na^{+}	5291
Cl^{-}	9947
SO_4^{2-}	1001

latter [19]. Acid SO_4-Cl brines can form (1) after the influx of volcanic gases, such as sulphur dioxide and sulphur trioxide, (2) by the reaction of oxygenated meteoric water in the vadose zone with hydrogen sulphide from geothermal steam, (3) by contact of neutral water with buried solfatara and acid minerals from relic solfatara, advanced argillic mineralisation in veins from an older system, near-surface pyrite oxidation and (4) by the influx of seawater and its heating to temperatures >300 °C, i.e. conditions in which magnesium in seawater precipitates as magnesium hydroxide and/or magnesium hydroxide sulphate hydrate, causing the pH to drop dramatically.

The corrosion behaviour of metals and alloys in highly acidic geothermal environments has received limited research attention. For example, the corrosion behaviour of common tubular materials suitable for use with H_2SO_4 fluids within the pH range of 2–4 is rarely studied across the open literature [20–23]. This knowledge gap constrains the selection of suitable materials for use at elevated temperatures and acidic conditions in this pH range and highlights the need for further research to ensure material reliability and performance.

Corrosion in H_2SO_4 solutions proceeds through the chemical dissociation of H_2SO_4, resulting in the production of hydrogen ions and bisulphate ions that further dissociate into sulphate ions, as shown in (1) and (2) [17]:

$$H_2SO_4 \rightarrow H^+ + HSO_4^- \quad (1)$$

$$HSO_4^- \rightarrow H^+ + SO_4^{2-} \quad (2)$$

As part of the corrosion reactions involving steel within H_2SO_4 environments, the iron within the steel oxidises into iron ions under anaerobic conditions [24–26]:

$$Fe_{(s)} \rightarrow Fe^{2+}_{(aq)} + 2e^- \quad (3)$$

Passivation can usually be observed when iron and carbon steels are exposed to highly concentrated H_2SO_4 environments. Studies have shown that protective layers can form on carbon steel when exposed to H_2SO_4 concentrations of 5 M to 10 M together with temperatures ranging from room temperature to 100 °C [27–29]. The protective films are attributed to the reactions between iron and sulphate ions forming iron sulphate ($FeSO_4$) when the local solubility limit is exceeded:

$$Fe^{2+}_{(aq)} + SO_4^{2-}{}_{(aq)} \rightarrow FeSO_4{}_{(s)} \quad (4)$$

Even at lower H_2SO_4 concentrations of around 1 M, metal dissolution rates are reduced because of the formation of a protective $FeSO_4$ layer [30,31]. However, within the pH range of 2–4 at elevated temperatures, the potential for the formation of protective layers is not well understood and represents a critical knowledge gap in terms of carbon steel behaviour in such environments. On one hand, if protective films can reduce corrosion rates on carbon steels, then these materials may be acceptable for use in specific low pH environments containing H_2SO_4. Otherwise, alternative materials should be considered. However, there is also limited information in relation to the behaviour of corrosion resistant alloys as alternative materials to carbon steel under these conditions. Studies indicate that lower dissolution rates are generally observed on stainless steels as opposed to carbon steels due to the presence of passive films consisting of Fe and Cr. However, in acidic environments, instability of the passive film and selective dissolution from the alloys may be identified [32–34].

Research with stainless steels highlights that corrosion resistance improves with increasing Cr content when exposed to sulphuric acid environments. Experiments conducted in room temperatures with stainless steels in sulphuric acid have indicated the presence of passive films composed of iron and chromium oxide/hydroxides, but stainless steels with high Cr content tend to have lesser film porosity and form very thin film layers on the surface of the materials [35,36]. Many discussions for stainless steels also characterise the nature of the passive film through polarisation measurements to explain the passive film breakdown and repassivity for the materials. Sulphuric acid

Table 2
Element compositions of N80 medium carbon steel, 13 Cr stainless steel (UNS S42000) and 2205 duplex stainless steel (UNS S32205) in weight % [43].

Material	Fe	C	Mn	P	S	Si	Cr	Mo	Cu	Ni
N80 medium carbon steel	98.3	0.24	1.19	0.011	0.013	0.22	0.036	0.018		
13 Cr stainless steel (UNS S42000)	85.6	0.2	0.9	0.16	0.02	0.27	12.67		0.01	0.16
2205 duplex stainless steel (UNS S32205)	67.8	0.02	1.21	0.023	0.001	0.44	22.5	3.05		4.99

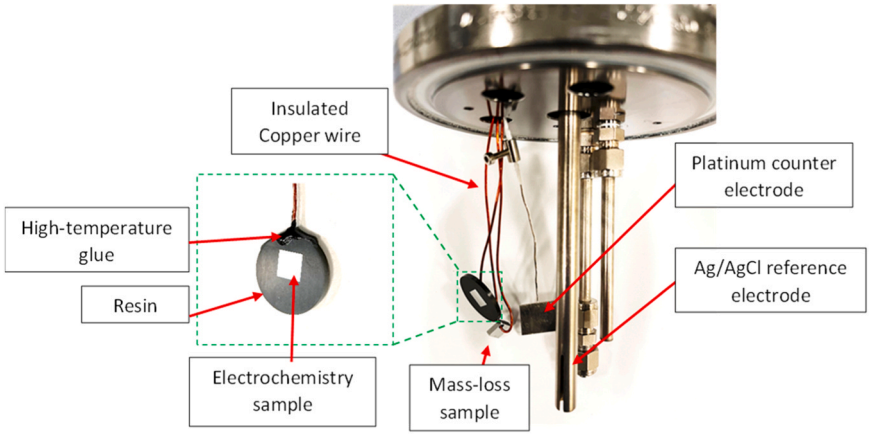

Fig. 1. Autoclave vessel cover consisting of three-electrode cell components and mass-loss sample.

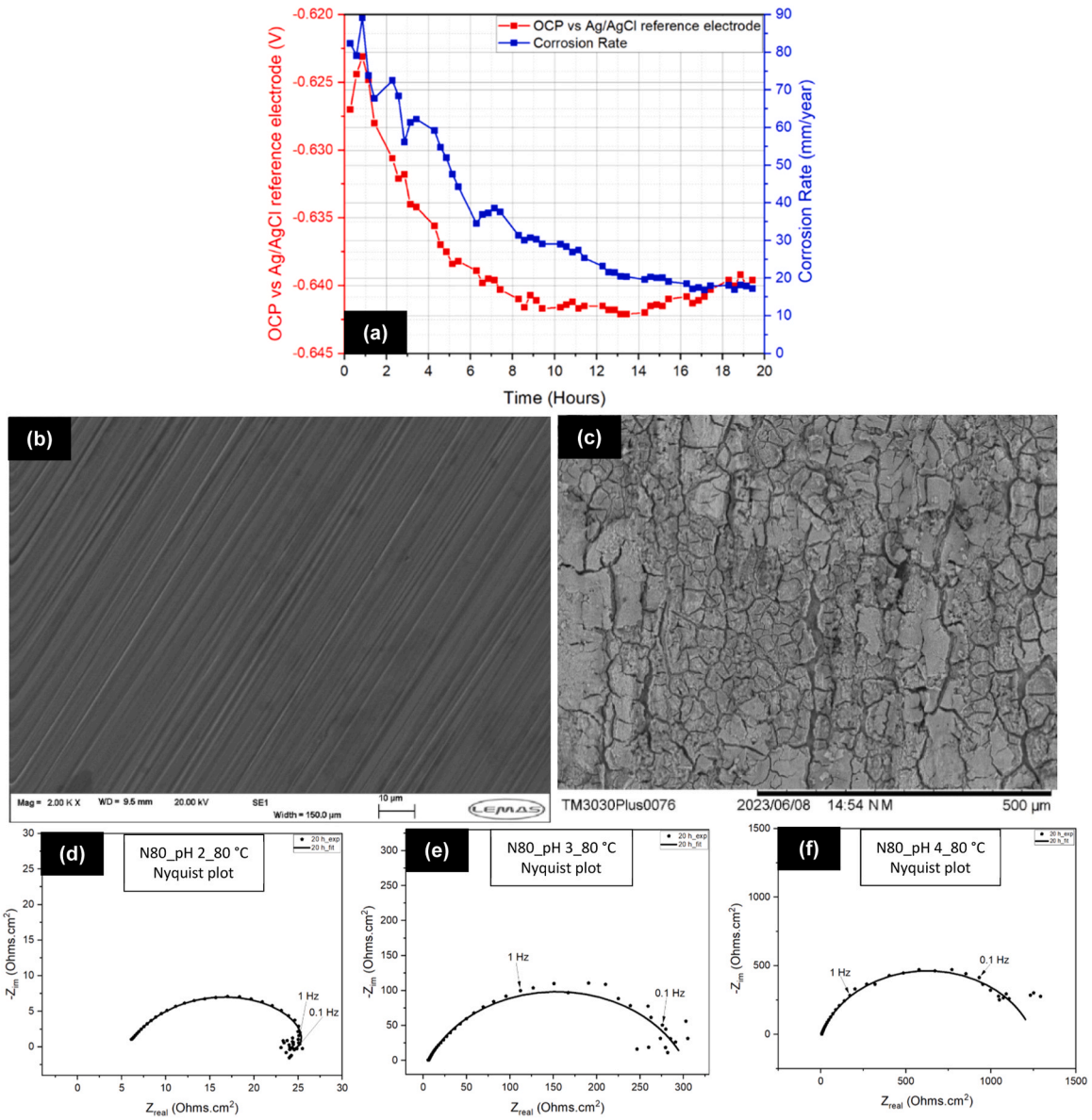

Fig. 2. (a) example of plotted open circuit potential (OCP) values and corrosion rates measured using linear polarisation resistance (LPR) over 20 h for N80 carbon steel in geothermal brine at pH 2 and 80 °C with observation of SEM image (b) before and (c) after experiment. With examples of impedance measurements (d) to (f) for N80 carbon steel in sulphuric acid environments.

environments with increased chloride ions are known to initiate pitting corrosion on stainless steels because of the breakdown of the passive films that can have reduced ability to repassivate in high-acid environments [37–40]. Although stainless steels are widely researched, there is not much visibility around the behaviour of stainless steels in high-temperature sulphuric acid environments that will simulate on-site geothermal environments.

Corrosion research within H_2SO_4 environments across high temperatures and pressures is nowhere near as comprehensive compared to carbon dioxide (CO_2) environments. Therefore, the purpose of this paper is to develop an understanding of the degradation mechanisms and likely corrosion rates of pipeline materials encountered in geothermal environments containing low pH H_2SO_4 [41,42].

This work implements a carefully developed test methodology to obtain a set of results for carbon steel and stainless steels (13 Cr and 22 Cr duplex stainless steel). Investigating the degree of corrosion across these materials in extreme conditions provides an opportunity to explore the performance of common materials. Importantly, understanding the behaviour of such materials creates a source of comparison with alternative material performances and potential chemical treatment strategies, hence aiming to support the implementation of corrosion management strategies across such geothermal systems.

2. Experimental procedure

2.1. Preparation of geothermal brine solution

The test solution comprised a 1 L H_2SO_4 brine solution to replicate an acid-sulphate-chloride geothermal fluid. Calcium Sulphate dihydrate ($CaSO_4.2H_2O$), Magnesium Sulphate ($MgSO_4$), Magnesium Chloride Hexahydrate ($MgCl_2.6H_2O$), Potassium Chloride (KCl) and Sodium Chloride (NaCl) were combined with 1 L distilled water (indicated within Table 1) and varying concentration of H_2SO_4 were used to adjust the pH of the test solution to specific values necessary for the test condition. The pH measurements were performed using an automatic temperature compensation (ATC) pH probe. The probe was calibrated

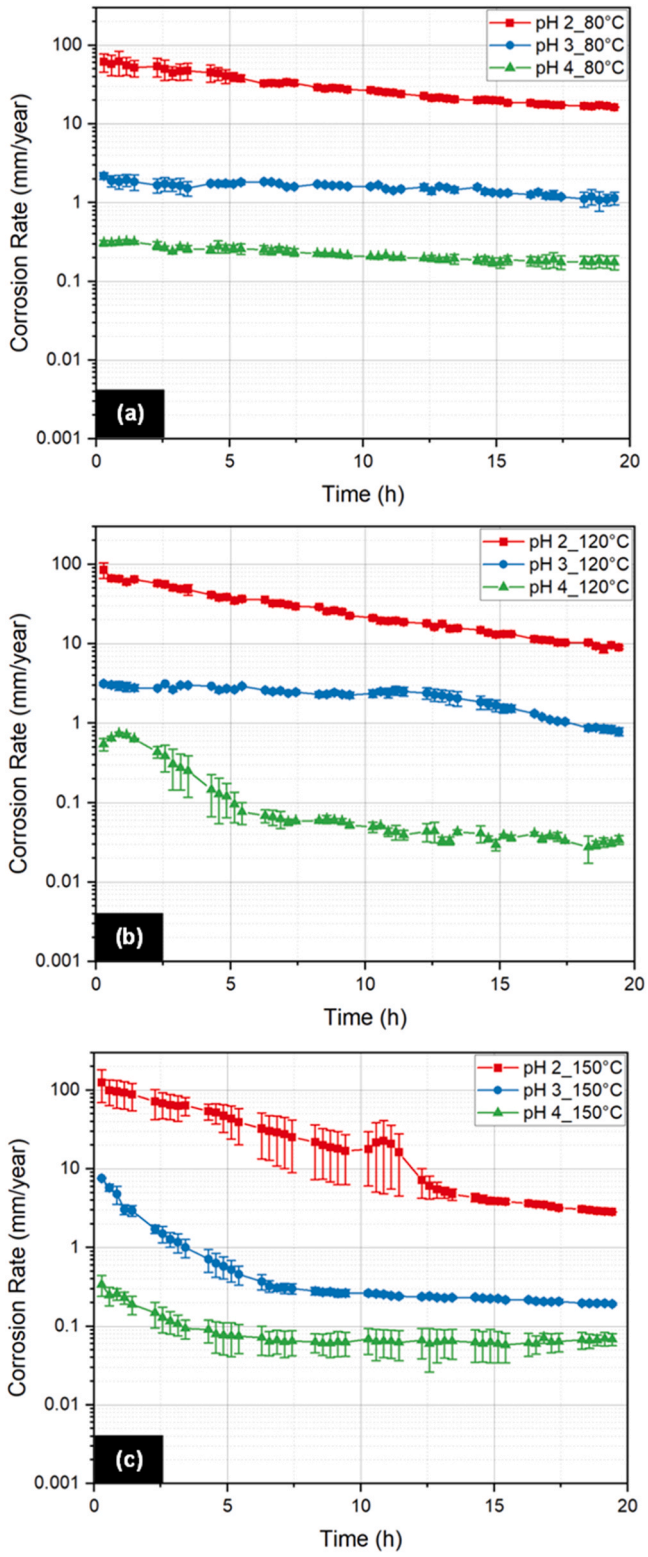

Fig. 3. Corrosion rates of N80 carbon steel determined from linear polarisation resistance (LPR) measurements over 20 h in geothermal brine at pH 2, 3 and 4 at test temperatures of (a) 80 °C, (b) 120 °C and (c) 150 °C.

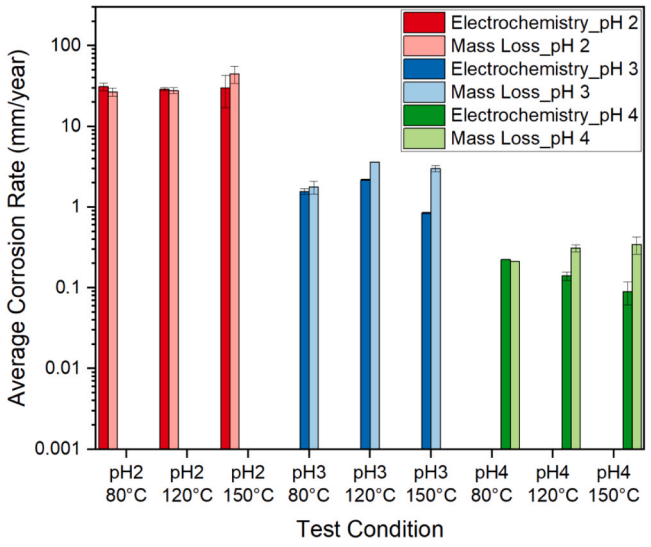

Fig. 4. Average electrochemistry and mass-loss corrosion rate comparisons of N80 carbon steel from 20 h experiments in geothermal brine solutions at pH 2, 3 and 4 at test temperatures of 80 °C, 120 °C and 150 °C.

with pH 1.68, 4 and 7 buffer solutions whilst bubbling the solution with Nitrogen (N_2) gas.

2.2. Material preparation

The N80 medium carbon steel, 13 Cr stainless steel (UNS S42000) and 2205 duplex stainless steel (UNS S32205) material samples (with material compositions given in Table 2) were cut into ~ 10 × 10 x 4 mm cuboids. The samples were prepared to collect two types of measurements. One set of samples had a 3 mm hole for suspending the sample and had a total surface area of ~3.4 cm^2 to use sufficient area for microscopic observations and mass loss measurements. In addition, another set of samples had an area of ~1 cm^2 to record real-time electrochemistry data while immersed in the solution.

The mass loss samples were suspended in the test solution with Kapton insulated wire, whereas the electrochemistry samples were prepared with a thermosetting resin by using a hot-compression mount. Moreover, the electrochemistry samples were attached to the Kapton insulated copper wire by feeding the copper wire through a small hole through the side of the resin until the wire was in contact with the sample. The interface between the wire and the resin was covered with a high-temperature glue that was cured in an oven at 120 °C for 2 h. The material samples were further prepared with a sequence of wet-grinding steps using P-grade silicon carbide grinding papers starting from P240 grit, then progressing to P400 grit, P800 grit and P1200 grit. Finally, the samples were cleaned with deionised water, followed by acetone and then dried.

2.3. Equipment setup

The prepared 1 L test solution was poured into a glass container and sealed. The solution in the glass vessel was bubbled with N_2 gas for a minimum of two hours to create an oxygen-free solution. A 1.3 L capacity tantalum-lined stainless steel autoclave vessel was used to prevent internal corrosion of the autoclave and subsequent contamination of the solution when testing with highly acidic fluids. The autoclave vessel cover was assembled with a carbon or stainless steel working electrode (depending on the experiment), platinum counter electrode (8 cm^2 surface area) and a silver/silver-chloride (Ag/AgCl) internal reference electrode (Fig. 1) with a standard electrode potential of + 0.210 V versus the standard hydrogen electrode to complete the

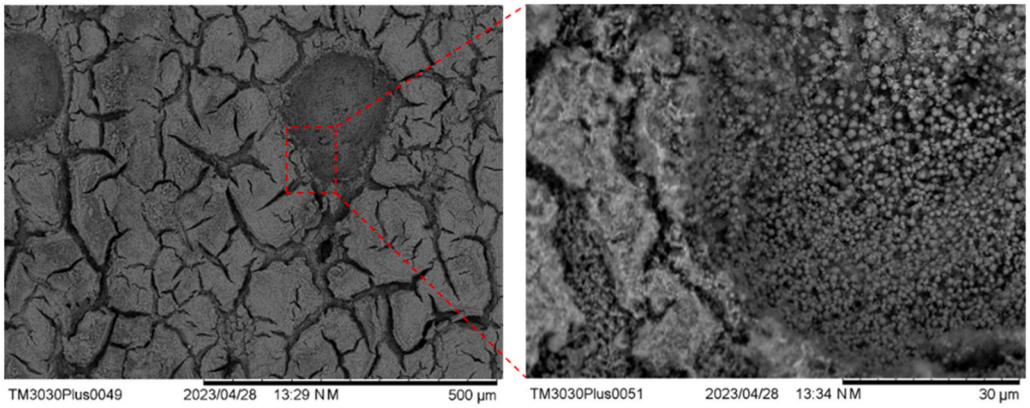

Fig. 5. SEM images of N80 medium carbon steel material from pH 2 and 150 °C test in geothermal brine.

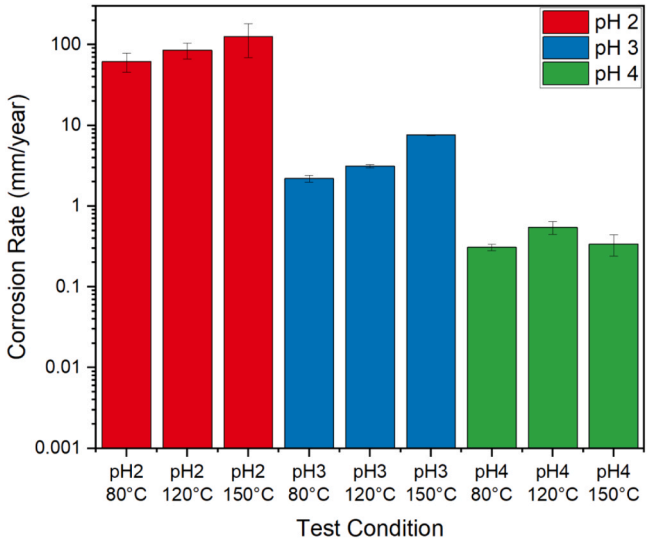

Fig. 6. Electrochemistry corrosion rates of N80 medium carbon steel recorded within 2 h period of test in geothermal brine solution.

three-electrode cell, allowing for *in-situ* electrochemistry measurements to be collected. Additionally, to collect mass loss data and conduct surface analysis, a mass loss sample was also included as seen in Fig. 1.

After aligning the material samples, the vessel cover was placed on the autoclave and sealed. The autoclave was purged with N_2 gas for 30 min to ensure minimal oxygen in the autoclave. With the use of a potentiostat, the electrode wire connections were attached to the working, counter and reference electrodes to facilitate electrochemical measurements.

In order to proceed with the corrosion tests, 700 mL of the test solution was transferred from the glass container to the autoclave, thus submerging the material samples into the test solution, and allowing room for thermal expansion of the aqueous phase. A hot-plate was used for heating the autoclave to the target temperatures of either 80 °C, 120 °C or 150 °C and a maximum pressure of 3.5 bar was maintained within the autoclave during the 150 °C experiments. All the corrosion tests were run for 20 h and inside the autoclave, a temperature probe from the hot-plate was immersed into a metal tube submerged in the test solution, at the same height as the test samples, in order to provide a reliable temperature reading.

2.4. Experimental measurements

The corrosion tests were evaluated using electrochemical linear polarisation resistance (LPR) and electrochemical impedance spectroscopy (EIS) measurements. The LPR responses were collected by scanning from −15 mV to + 15 mV relative to the open circuit potential (OCP) of the material at a scan rate of 0.25 mV/s for the carbon steel and 0.1 mV/s for the stainless and duplex steels. EIS measurements were completed within a frequency range scanning from 20000 Hz to 0.01 Hz at a potential of ±15 mV. LPR measurements for the 13 Cr and 22 Cr materials were recorded with a lower scan rate because by applying a higher scan rate, the forward and backward scans for the LPR showed a hysteresis due to the passive characteristics of the materials, hence the scan rate was reduced. Stern-Geary coefficients ranging between 21 mV/decade and 26 mV/decade were recorded from Tafel polarisation measurements and each coefficient was applied accordingly to the given system corresponding to pH 2, 3 and 4. Using the obtained polarisation resistance values and Stern-Geary coefficient, the corrosion current densities were calculated with the Stern-Geary Eq. (5), where i_{corr} is corrosion current, R_p is the gradient on a potential-current graph that is corrected with compensation of the solution resistance from the EIS measurements, β_a and β_c are Tafel constants as part of the Stern-Geary coefficient (B).

$$i_{corr} = \frac{1}{R_p}\left(\frac{\beta_a \beta_c}{2.303(\beta_a + \beta_c)}\right) = \frac{1}{R_p} \times (B) \tag{5}$$

Acceptance of using (5) was based on the conditions that high excitation voltages were not used, polarisation voltages were not held for long periods of time and occurrences of adsorption pseudo-capacitance were not observed from these experiments [44].

Moreover, the corrosion rates in units of mm/year were calculated with the following equation:

$$Corrosion\ Rate(CR) = \frac{i(EW)}{\rho FA} \tag{6}$$

where i is corrosion current in units of Amps, EW is equivalent weight known from the material properties containing units of g/equivalent, ρ is material density in units of g/cm^3, F is Faraday's constant with units of Coulombs/mole and A is the exposed material area in the solution in units of cm^2.

Regarding the mass-loss samples, mass was recorded using a mass balance accurate to 0.01 mg. Mass values were collected before the corrosion experiment (initial mass) and after the experiment the sample mass was recorded with and without corrosion products (final mass). Based on mass-loss data corrosion rate in mm/year was calculated with the following equation:

$$Corrosion\ Rate(CR) = k\left(\frac{m_{loss}}{\rho t A}\right) \tag{7}$$

where k is a conversion factor equal to 3.1536×10^8, m_{loss} is the

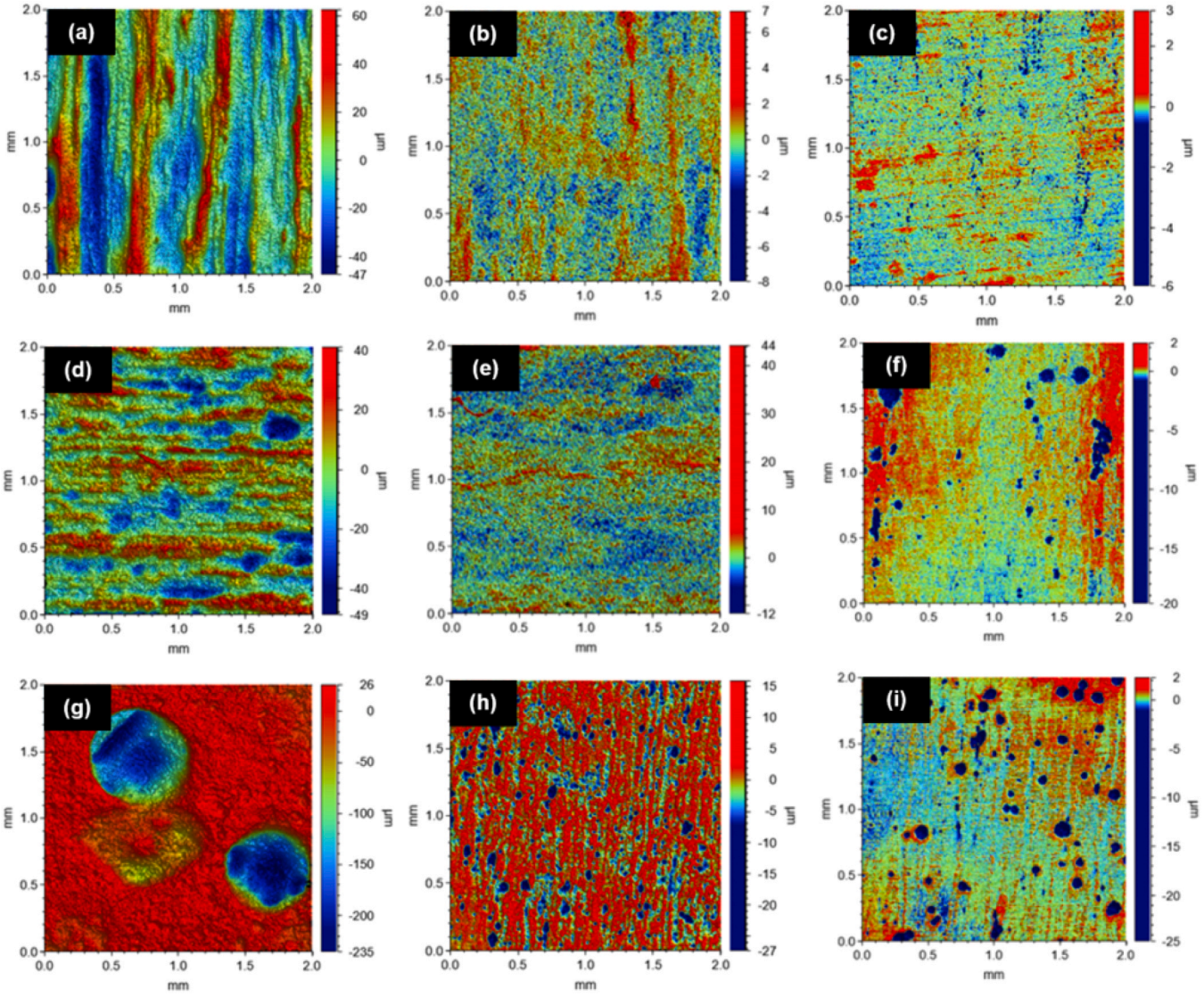

Fig. 7. Surface profiles with corresponding scale bars to indicate localised effects for N80 material for tested conditions (a) pH2 80 °C, (b) pH3 80 °C, (c) pH4 80 °C, (d) pH2 120 °C, (e) pH3 120 °C, (f) pH4 120 °C, (g) pH2 150 °C, (h) pH3 150 °C, (i) pH4 150 °C. (Note: Scale bars for each surface profile is different).

difference between initial and final sample mass in units of g and t is exposure time in units of seconds.

Hence, the average corrosion rate in mm/year for the 20 h exposure period was calculated with the following equation:

$$Average\ Corrosion\ Rate = \frac{Sum\ of\ corrosion\ rate\ values}{Total\ number\ of\ corrosion\ rate\ values} \quad (8)$$

The corrosion products on the material were removed with a hydrochloric acid solution mixed with hexamethylenetetramine corrosion inhibitor [45]. Additionally, after the experiment, the test solution was allowed to naturally cool to room temperature whilst bubbling with N_2 before measuring pH again with the ATC probe to determine the degree of acid consumption during the experiment.

After 20 h of testing, the stainless and duplex steel samples were additionally evaluated with electrochemical cyclic potentiodynamic polarisation (CPP) measurements. CPP plots were obtained by polarising the material from −5 mV relative to the OCP at a scan rate of 1 mV/s with a reversal current of 5 mA/cm^2.

Initial experiments with the N80 carbon steel were conducted with low-pH solutions of pH 2, 3 and 4 at elevated temperatures of 80 °C, 120 °C and 150 °C. In comparison, the UNS S42000 stainless steel and UNS S32205 duplex steel were subjected to the low-pH solutions only at 150 °C to observe material performance under the most aggressive environments.

2.5. Surface characterisation

Corroded samples were observed with a Hitachi TM3030Plus Bench Top Scanning Electron Microscope (SEM) and a Carl Zeiss EVO MA15 SEM, using secondary electron imaging signal with 20 kV accelerating voltage and a working distance between 8 mm and 10 mm. Furthermore, material regions with localised corrosion were analysed with a Bruker NPFlex white light interferometer to obtain 3D surface profiles of the corrosion features. A Tescan – Amber X Dual beam plasma focused ion beam (PFIBSEM) and a FEI – Helios G4 CX Dual beam FIBSEM were utilised to cut cross-sections of the material sample tilted at ~54° relative to the electron beam axis and SEM images were captured with 2 kV voltage and 100 pA current. As part of the post-test material analysis energy dispersive x-ray spectroscopy (EDX) was also used to identify elemental composition of the corroded samples. Additionally, a Bruker D8 diffractometer was used for collecting X-ray diffraction (XRD) spectrums within a 2 θ scan range of 20 ° to 70 ° at a step size of 0.032 °/s.

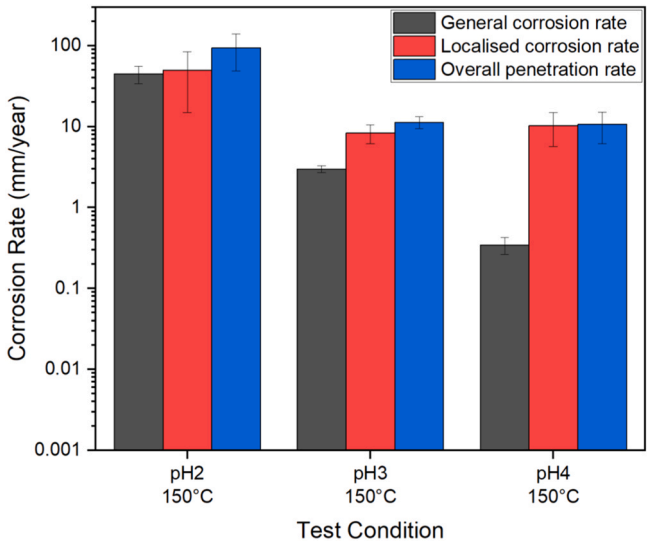

Fig. 8. Bar chart showing general corrosion rate, localised corrosion and overall penetration rate of N80 carbon steel tested in pH 2, 3 and 4 geothermal brine solutions at 150 °C.

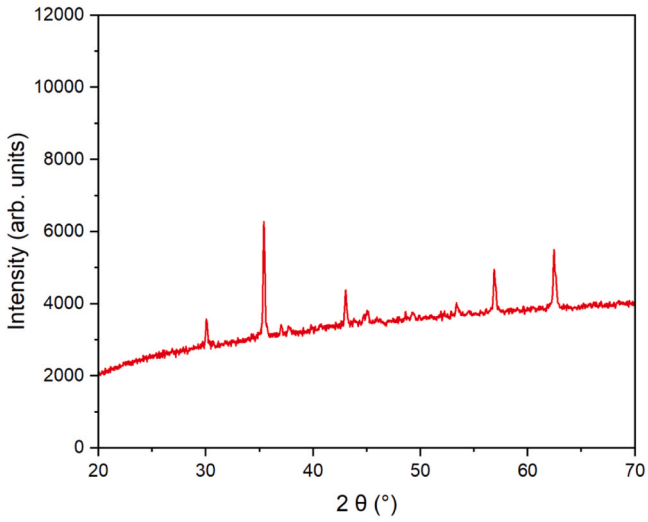

Fig. 10. XRD pattern of N80 material exposed to pH 2 H_2SO_4 solution at 150 °C, indicating Fe_3C revealed on the corroded material surface.

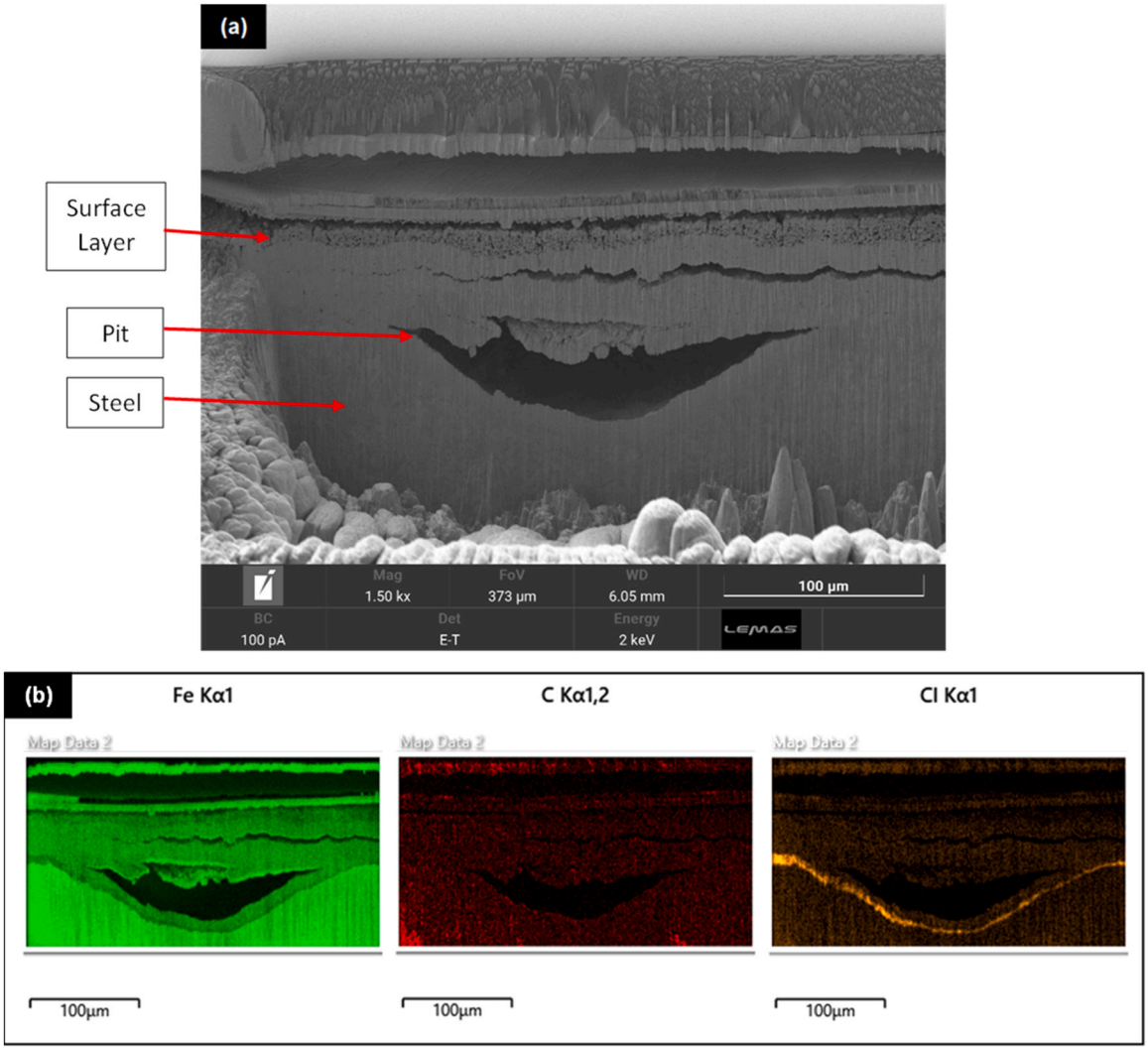

Fig. 9. Plasma focused ion beam (PFIB) of (a) cross-sectioned N80 medium carbon steel SEM and (b) EDX image from pH 2 geothermal brine and 150 °C test to observe geometry of localised corrosion feature.

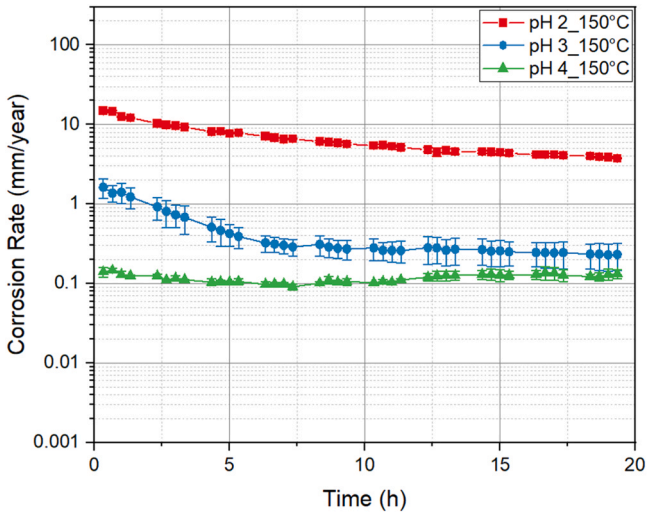

Fig. 11. Corrosion rates of 13 Cr stainless steel (UNS S42000) determined from LPR measurements during 20 h in geothermal brine at pH 2, 3 and 4 and a test temperature 150 °C.

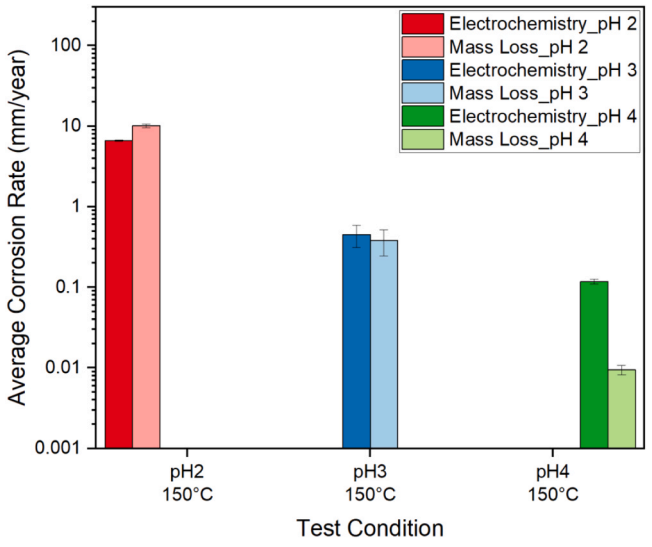

Fig. 12. Average electrochemistry and mass-loss corrosion rate comparisons of 13 Cr stainless steel (UNS S42000) from 20 h experiments in geothermal brine solutions at pH 2, 3 and 4 at test temperature 150 °C.

3. Results

3.1. N80 carbon steel corrosion rates as a function of temperature and pH

A series of experiments were carried out on N80 carbon steel exposed to low-pH solutions (pH 2, 3 and 4) and elevated temperatures (80 °C, 120 °C and 150 °C). An example of the LPR measurements and complementary SEM image is shown in Fig. 2. This response is reflective of other conditions in that the corrosion rate drops with respect to time, which needs to be understood and is considered in the following sections. Corrosion effects on the carbon steel material were evidenced with the SEM image to portray the presence of surface products. Plus, Fig. 2 also provides examples of impedance plots for the N80 carbon steel in sulphuric acid solutions measured at the 20 h mark of the tests. Impedance data for the low-pH conditions generally indicated a single capacitive loop throughout the test duration. However, for the pH 2 condition an inductive loop was present which was insignificant in the calculation.

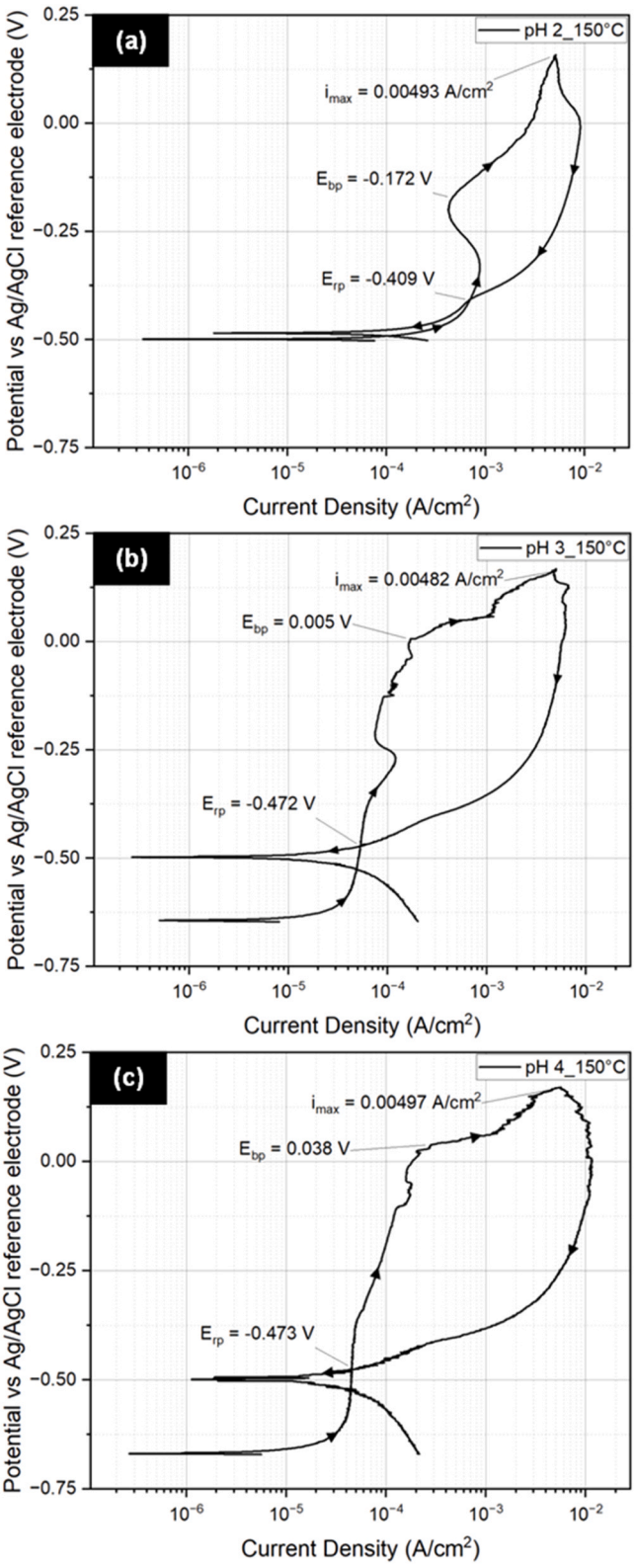

Fig. 13. CPP plots of 13 Cr stainless steel (UNS S42000) measured after 20 h in geothermal brine at (a) pH 2, (b) pH 3 and (c) pH 4 at test temperature 150 °C.

Similarly, subsequent experimental results were collected under different test conditions in order to compare the performance of carbon steel across elevated temperatures and low-pH geothermal environments. As shown in Fig. 3, carbon steel corrosion in pH 2 solutions showed an increase in the rate of dissolution from 65 mm/year to

Table 3
Data from 13 Cr stainless steel (UNS S42000) CPP plots at 150 °C.

13 Cr stainless steel (UNS S42000)	pH 2	pH 3	pH 4
E_{bp} (V)	−0.172	0.005	0.038
E_{rp} (V)	−0.409	−0.472	−0.473
i_{max} (A/cm^2)	0.00493	0.00482	0.00497
$E_{bp} - E_{rp}$ (V)	0.237	0.477	0.511

133 mm/year as temperature was increased from 80 °C to 150 °C. At pH 3, corrosion rate increased from 3 mm/year and 9.5 mm/year as temperature increased over the same range. Finally, carbon steel corrosion rates only increased from 0.3 mm/year to 0.5 mm/year with a temperature increased from 80 °C to 150 °C. Examination of the results for the 150 °C experiments indicated that the initial corrosion rate was 132.7 ± 59 mm/year with the pH 2 solution, 9.4 ± 0.1 mm/year with the pH 3 solution and 0.3 ± 0.1 mm/year with the pH 4 solution. Thus, the results in Fig. 3 illustrate that for a given temperature, the corrosion rates increase by nearly one order of magnitude as the pH of the solution decreases by one unit. The plotted error bars represent the maximum and minimum values from two corrosion rate measurements.

The LPR measurements showed that the corrosion behavior of the carbon steel was predominantly influenced by the acidicty of the solution, with elevation in temperature playing a comparatively minor role within the considered range evaluated. Closer examination of this trend in Fig. 3 showed that the initial corrosion rate at the 2 h mark for the 80 °C, pH 2 solution was 65.2 mm/year and for the 120 °C, pH 2 solution the initial corrosion rate was 90.6 mm/year, hence displaying an almost 30 % difference in corrosion rate with respect to temperature increase. On the other hand, for the 120 °C tests the corrosion rates varied by approximately an order of magnitude when comparing pH 3 to pH 2.

An overview of the average corrosion rates comparatively measured with the electrochemistry and mass-loss techniques illustrated a good correlation of results. As observed in Fig. 4, the corrosion behaviour of N80 carbon steel was more severe with the pH 2 conditions than with the pH 3 and pH 4 conditions. Moreover, the indication of similar average corrosion rate values obtained with the electrochemistry and mass-loss techniques provided good confidence for the development of a valid experimental electrochemical methodology.

3.1.1. Examining the reduction in corrosion rate with time for N80 experiments

The recorded corrosion rates were seen to decrease during the 20 h test period, more closely obvious in Fig. 3(c). This response was investigated further through developing an understanding in relation to pH changes within the test solution, as well as the formation of potential corrosion products on the steel surface particularly at lower pH experiments where the formation of protective scale (such as various iron oxides and $FeSO_4$) is reportedly more prevalent.

For the 150 °C experiments the pH of the bulk test solution measured at room temperature at the beginning of the experiments were adjusted accordingly to pH 2, 3 and 4, but at the end of the tests the pH values of the test solution measured at room temperature differed by either four or five units from their original value, highlighting a high degree of acid consumption in each experiment. Obervations from the 150 °C experiments indicated that with an initial pH 2 solution the final pH measured after 20 h at room temperature was pH 5 ± 0.9. With an initial pH 3 solution, the final pH measured was pH 7 ± 0.1 and with an initial pH 4 solution, the final pH measured was pH 9 ± 0.1. Relatviely similar increases in pH were observed from the 80 °C and 120 °C experiments. The difference in pH values between the start and end of the experiment indicates that a substantial level of H^+ ions were consumed during the experiment. As the pH of the solution increased, acidity levels were substantially reduced and the corrosion rates clearly decrease.

The N80 carbon steel material experienced the greatest corrosion while exposed to the pH 2 solution at 150 °C. Microscopic observations of the corroded carbon steel material as in Fig. 5 showed the presence of a nano-polycrystalline surface morphology, possibly revealed from the material microstructure [26,46,47]. Under the aggressive test conditions of the pH 2 solution at 150 °C the surface morphology shown in Fig. 5 does not protect the metal from corrosion. This was concluded from separate experiments where a fresh sample was placed into the used test solution and shown to provide similar corrosion attack as experienced by the used sample.

These results confirm that the initial, highest corrosion rates measured electrochemically from the 20 h period are more appropriate to express an understanding for the corrosion behaviour of the carbon steel in a geothermal environment where the conditions are at a relatively steady state. As such, Fig. 6 illustrates the initial corrosion rate values from the graphs in Fig. 3 to provide an improved representation

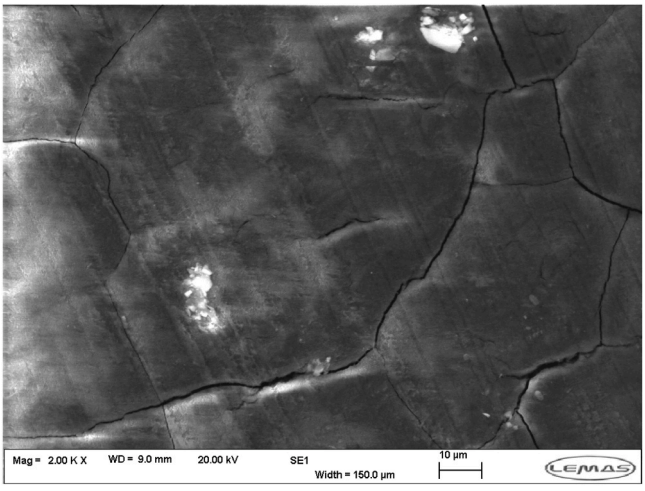

Fig. 15. SEM image of 13 Cr stainless steel (UNS S42000) from pH 2 and 150 °C test in geothermal brine.

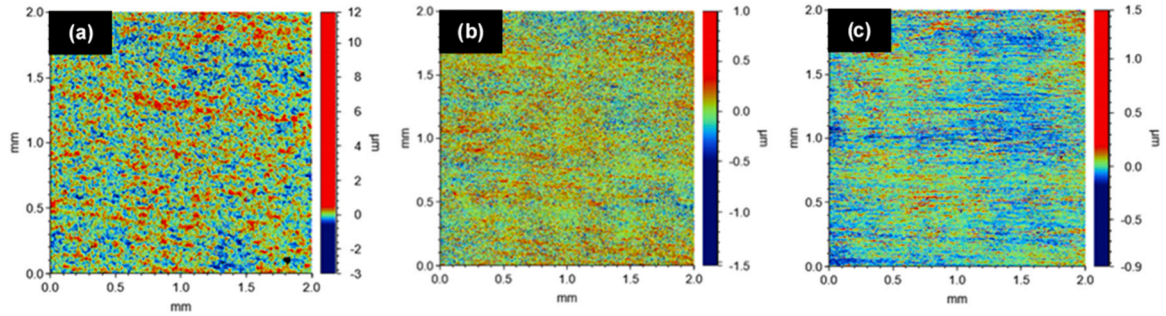

Fig. 14. Surface profiles with corresponding scale bars to indicate localised effects for 13 Cr stainless steel (UNS S42000) tested at 150 °C with (a) pH 2, (b) pH 3 and (c) pH 4 solutions.

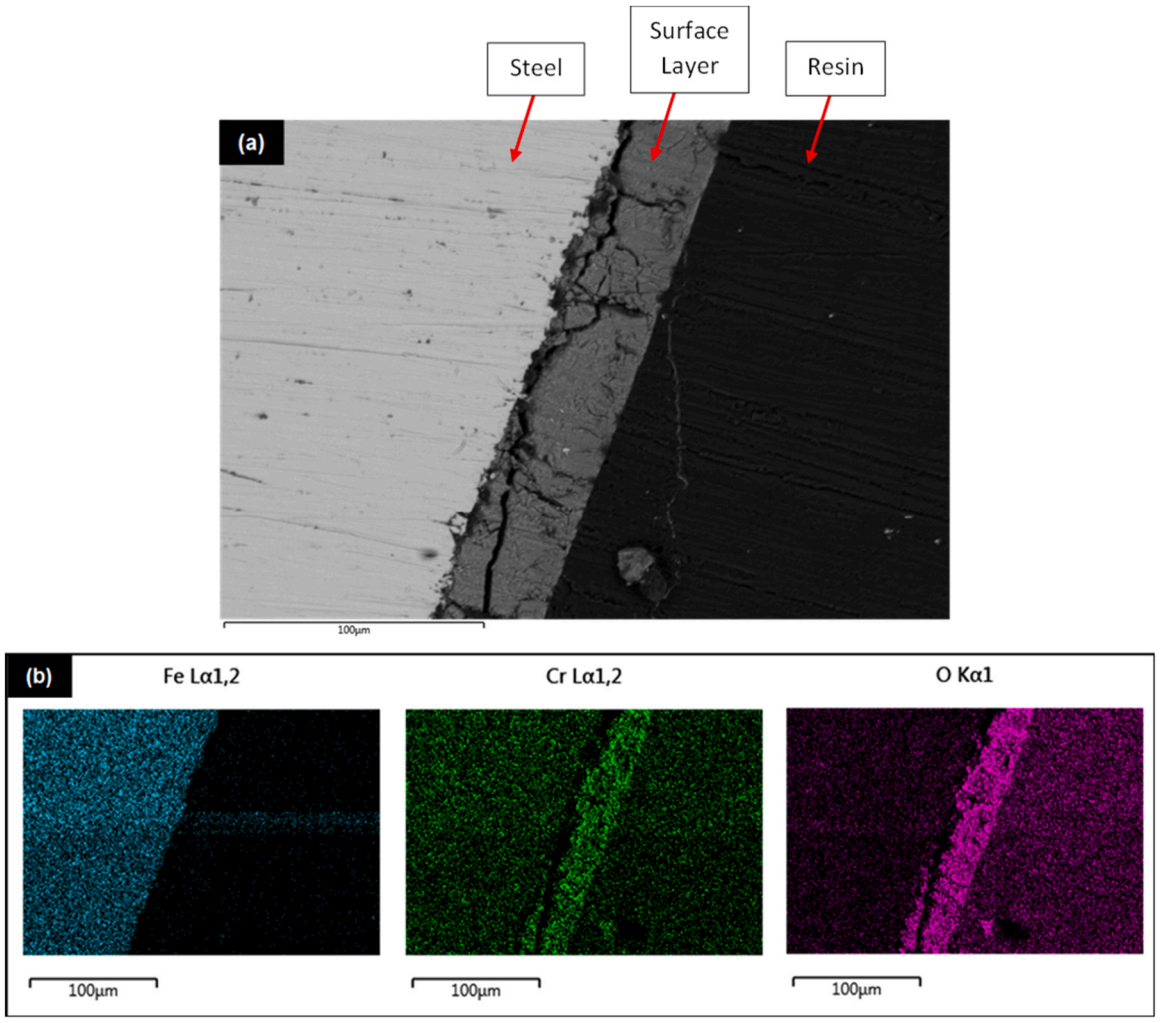

Fig. 16. (a) SEM image of cross-sectioned 13 Cr stainless steel (UNS S42000) and (b) EDX image from pH 2 geothermal brine and 150 °C test.

of the material behaviour within these elevated temperatures and low-pH conditions. Additionally, Fig. 6 highlights that in terms of the tested conditions solution pH has a large effect on corrosion compared to the small effects observed from test temperatures.

3.1.2. Analysing the impact of localised corrosion for N80 experiments

The results within this paper clearly demonstrated high corrosion rates with the N80 carbon steel in terms of general corrosion within the extreme test conditions (pH 2 and 150 °C). However, together with general corrosion, localised corrosion can have a significant impact on carbon steel materials [48]. Showing an appreciation for the general and localised corrosion on carbon steel can therefore support the motivation to establish a detailed understanding of the corrosion mechanism.

Signs of potential localised corrosion on the carbon steel were speculated with the SEM images, therefore a quantitative post-test analysis was performed with the Bruker NPFlex white light interferometer, on the tested material after corrosion product removal to evaluate the extent of localised corrosion on the N80 carbon steel exposed to the different tested conditions. As identified in Fig. 7, the carbon steel clearly underwent large amounts of material degradation, with localised corrosion features observed close to 200 µm depth.

In Fig. 7 the surface profiles of the corroded carbon steel were gathered for the tested conditions to analyse the effects of localised corrosion. The carbon steel was seen to have experienced greater localised corrosion in the pH 2 solutions and when tested at 150 °C. Therefore, the combination of general and localised corrosion on the carbon steel emphasises the severe corrosive nature of elevated temperature and low-pH geothermal environments.

The surface profiles for the N80 carbon steel tested at 150 °C were further analysed to obtain statistical data in terms of general and localised corrosion. As noticed in Fig. 8, general corrosion rates were plotted with comparison to the localised corrosion rates and together shown to determine an overall corrosion rate for the carbon steel. General corrosion rates were plotted by calculating an average of the mass loss measurements collected during 20 h experiments. Localised corrosion rates were obtained by identifying the ten deepest pits from the surface profile images and by calculating the average pit depths the localised corrosion rates were recorded with the assumption that the pit growth rate was constant. As a result the overall 'penetration rate' for each condition at 150 °C were plotted as the sum of the general and localised corrosion rates. The N80 carbon steel in the pH 3 and pH 4 solutions showed similar corrosive behaviour, but in the pH 2 solution the carbon steel indicated very high corrosion rates when considering both the localised and general corrosion rates.

Cross-sectioning the carbon steel tested in the pH 2 solution at 150 °C indicated a wide and shallow localised corroded region as shown in Fig. 9. EDX analysis for the cross-sectioned region indicated iron and carbon within the majority of the cross-sectional area, along with a layer of chloride ions present at the bottom of the locally corroded feature, signifying the mechanism of a stable pit nucleated on the carbon steel within the low pH solution. The accumulation of iron and chloride ions at the bottom of the propagated pit suggests that the production of metal

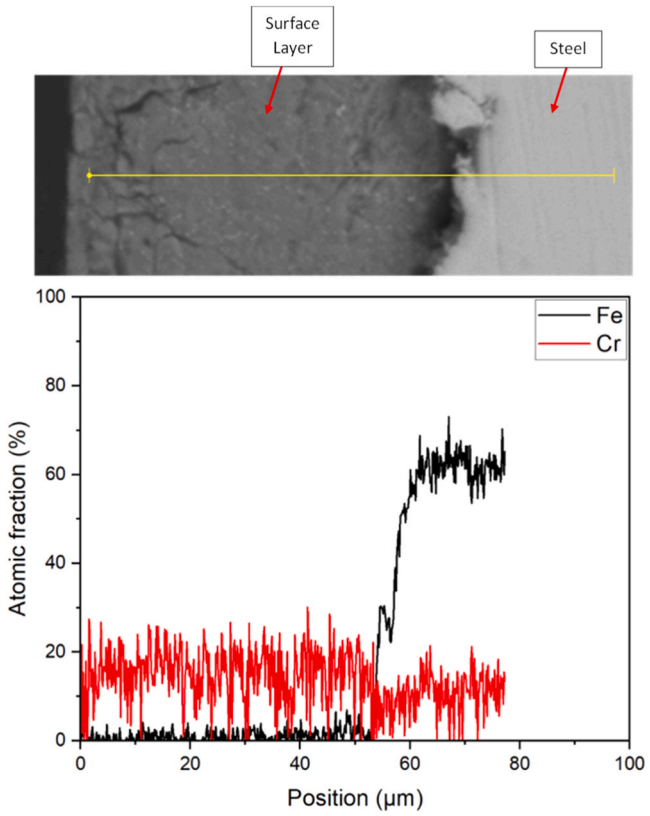

Fig. 17. Graphical data of the 13 Cr stainless steel (UNS S42000) from pH 2 geothermal brine and 150 °C test showing the changes in the amount of iron (Fe) and chromium (Cr) ions present within the material cross-section.

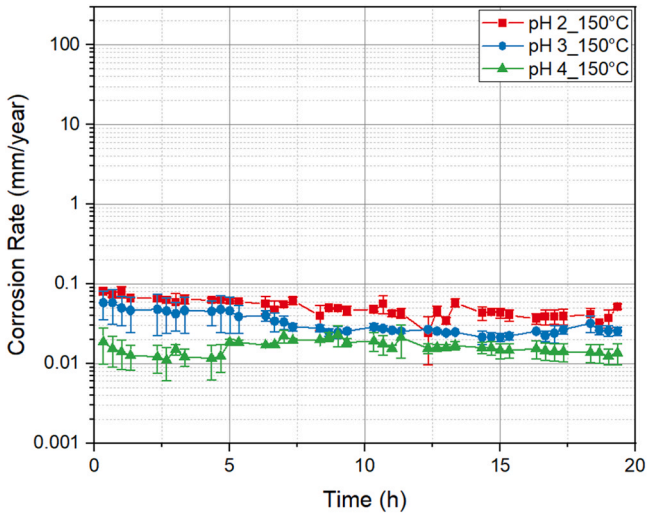

Fig. 18. Corrosion rates of 2205 duplex stainless steel (UNS S32205) determined from LPR measurements over 20 h in geothermal brine at pH 2, 3 and 4 at test temperature 150 °C.

ions through corrosion occurred at a much quicker rate than the rate at which the metal ions escaped from the metal, resulting in the formation of a salt layer. Therefore, the corroded region experienced supersaturation such that increased corrosion activity occurred within localised areas, hence causing the salt layer to develop [49,50]. In addition, it should be noted that although the test solution was mixed with H_2SO_4 to attain a solution pH of 2, the analysed cross-section of the carbon steel did not show any obvious presence of sulphur, therefore suggesting that

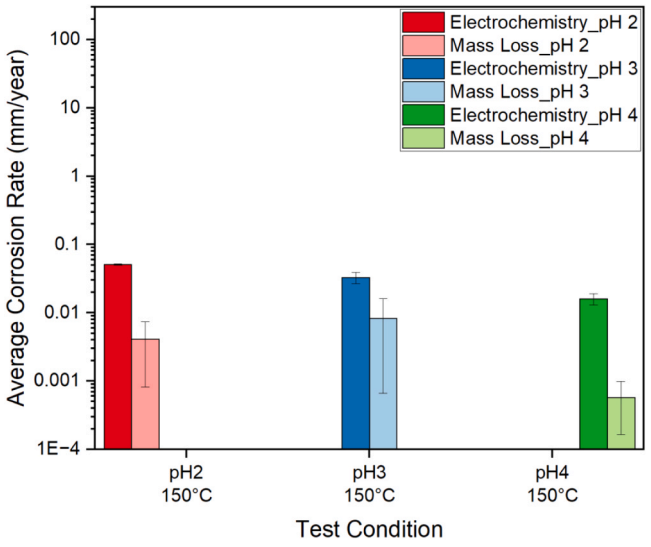

Fig. 19. Average electrochemistry and mass-loss corrosion rate comparisons of 2205 duplex stainless steel (UNS S32205) from 20 h experiments in geothermal brine solutions at pH 2, 3 and 4 at a test temperature 150 °C.

expected protective films such as $FeSO_4$ were not formed at this particular interface.

Moreover, XRD analysis of the N80 material tested in the pH 2 solution (Fig. 10) indicated diffraction peaks associated with iron carbide (Fe_3C), supported with the International Centre for Diffraction Data (ICDD) reference for Fe_3C (00–003–1056) peaks. Highest intensity peak for the Fe_3C was observed at a 2 θ value of 35 °, hence representing a layer revealed from within the N80 carbon steel microstructure itself [46].

3.2. 13 Cr stainless steel (UNS S42000)

Corrosion rates for 13 Cr stainless steel (UNS S42000) were investigated at 150 °C in pH 2, 3 and 4 geothermal brine solutions. At the end of the 20 h test, 13 Cr experienced average corrosion rates of nearly 7 mm/year in the pH 2 solution, 0.6 mm/year in the pH 3 solution and 0.1 mm/year in the pH 4 solution as illustrated in Fig. 11. Whilst subjected to the pH 2 and pH 3 solutions 13 Cr undergoes high corrosion activity, whereas in the pH 4 solution 13 Cr displays 'acceptable' performance with relatively low corrosion rates of 0.1 mm/year [51]. Fig. 11 also illustrates the decrease in corrosion rate over time for the 13 Cr material at pH 2 and 3. The decrease is most substantial at pH 2 and can be attributed predominantly to the establishment of a semi-protective layer with time. This can be concluded when considering that the final solution pH after 20 h of testing in the pH 2 solution remained at pH 2 ± 0.1. However, with regards to the pH 3 solution, the final test solutions reached significantly higher pH values than the starting values, suggesting acid consumption will have at least partly played a role in the reduction in corrosion rate with time at this condition.

Supported with the average corrosion rate results, Fig. 12 further indicates the severe material degradation occurring for the 13 Cr material in the pH 2 solution with similar results collected with the electrochemical and mass-loss techniques. Corrosion rates close to 10 mm/year were observed with the 13 Cr stainless steel in the pH 2 solution and < 1 mm/year on average when tested in the pH 3 and pH 4 solutions.

Fig. 13 cyclic potentiodynamic polarisation plots illustrate the active-passive film behaviour of the 13 Cr material when subjected to the low-pH solutions at 150 °C temperature with labelled values of the maximum current density (i_{max}), film breakdown potential (E_{bp}) and film repassivation potential (E_{rp}). From Fig. 13 and Table 3, the 13 Cr

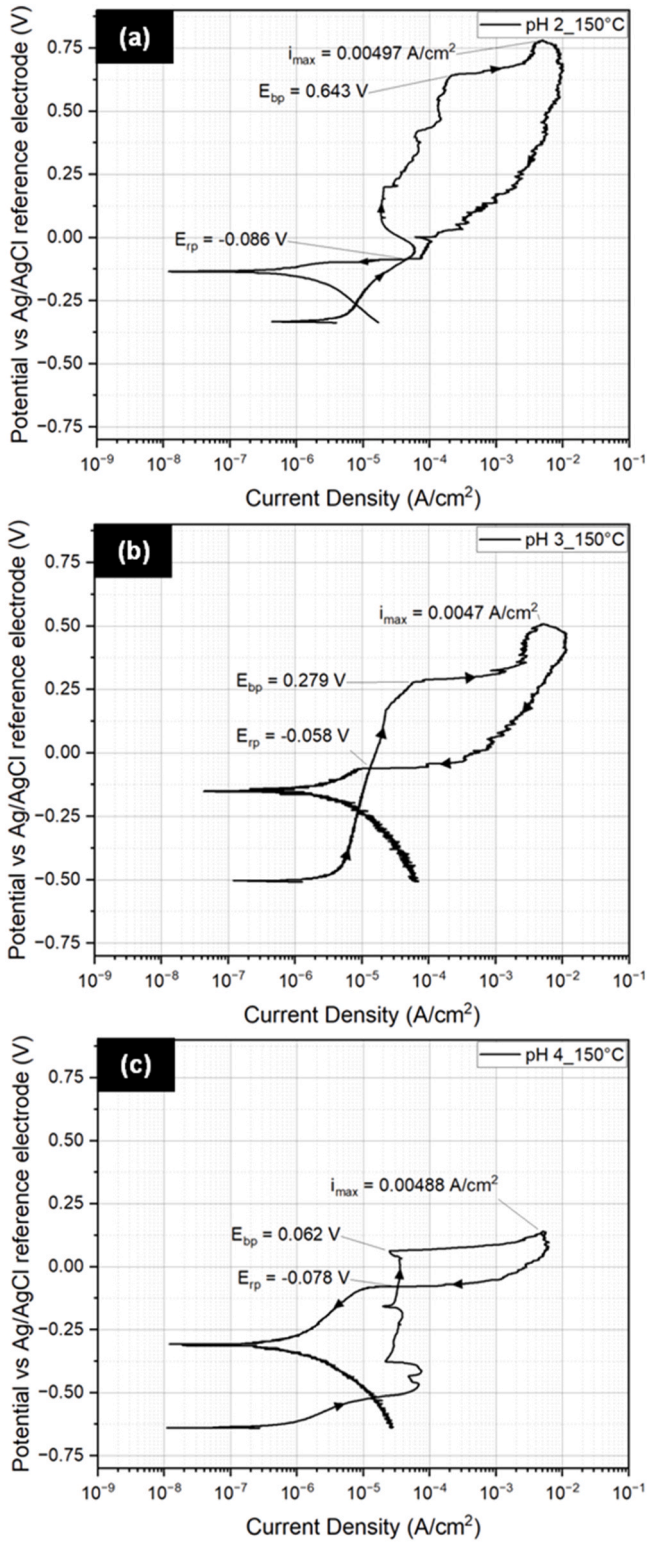

Fig. 20. CPP plots of 2205 duplex stainless steel (UNS S32205) measured after 20 h in geothermal brine at (a) pH 2, (b) pH 3 and (c) pH 4 at test temperature 150 °C.

stainless steel indicated lower E_{bp} values as the solution pH decreased, but as seen with Fig. 13 (a) it is challenging to determine clear E_{bp} values from the CPP plot because of the 13 Cr actively corroding in low-pH environments. 13 Cr stainless steel operating in pH 3 and pH 4 H_2SO_4 solution displays more pitting resistance than in the pH 2 solution and repassivation across the different conditions occurs within the −0.400 V and −0.475 V range.

Table 4
Data from 2205 duplex stainless steel (UNS S32205) CPP plots at 150 °C.

22 Cr duplex steel (UNS S32205)	pH 2	pH 3	pH 4
E_{bp} (V)	0.643	0.279	0.062
E_{rp} (V)	−0.086	−0.058	−0.078
i_{max} (A/cm^2)	0.00497	0.00470	0.00488
$E_{bp} - E_{rp}$ (V)	0.729	0.337	0.140

Presented in Fig. 14, the surface profiles captured for the 13 Cr material shows more physical degradation when exposed to the pH 2 H_2SO_4 solution at 150 °C, compared to minimal differences observed in material appearance when tested in the pH 3 and pH 4 solutions.

Surface observation (Fig. 15) of the 13 Cr material tested in the pH 2 solution evidenced the presence of a semi-protective film, as discussed previously, which resulted in the decrease in corrosion rate from 15 ± 0.5 mm/year to 3 ± 0.1 mm/year in the space of the 20 h experiment noted from Fig. 11.

A cross-section of the 13 Cr material tested in the pH 2 solution confirmed the presence of a porous chrome-rich layer formed uniformly on the surface of the stainless steel as shown in Fig. 16. Also, the chrome-rich layer was identified to have a thickness of around 40 μm. So, although the 13 Cr stainless steel portrayed relatively better corrosion resistance than the N80 medium carbon steel, the 13 Cr material still experienced high corrosion rates of more than 1 mm/year in the pH 2 geothermal brine solution.

Moreover, closer examination of the layer formed on the 13 Cr stainless steel indicated some preferential dissolution of metal ions from the bulk material. Supported with data from the 13 Cr cross-section after the 20 h experiment, Fig. 17 represents the elemental composition detected within the cross-section in terms of atomic fraction with units of %. Analysis of the 13 Cr cross-section showed almost no presence of iron (Fe) ions in the surface layer and nearly 60 % of Fe ions located in the steel, therefore explaining the dissolution of Fe ions taking place as a result of the corrosion reactions occurring at a high rate in the pH 2 solution. Additionally, across the 13 Cr cross-section 20 % of chromium (Cr) ions were captured from the surface layer and 10 % of Cr ions detected in the steel, therefore highlighting the presence of a Cr rich layer formed due to exposure of the bulk material in the H_2SO_4 solution [52].

3.3. 2205 duplex stainless steel (UNS S32205)

As a final comparison, 2205 duplex stainless steel (UNS S32205) was evaluated at 150 °C across the three pH values considered. The material produced corrosion rates < 0.1 mm/year in the pH 2 solution, as shown in Fig. 18. For the duplex steel, the initial corrosion rates within the pH 2 solution was 0.09 mm/year, with the pH 3 solution rates were 0.07 mm/year and with the pH 4 solution the rate was 0.02 mm/year. Hence indicating that with the UNS S32205 duplex steel, low corrosion rates are achieved across the pH range 2–4 with minimal difference in corrosion rates with changes in pH at 150 °C.

The average corrosion rates for the 22 Cr material, as shown in Fig. 19, demonstrates that the electrochemistry measurements provide an over-estimate compared to mass-loss measurements, but confirms that all corrosion rates were below 0.1 mm/year when 22 Cr material is exposed to H_2SO_4 geothermal solutions at 150 °C across a pH range of 2–4. Therefore, clearly highlighting that the 22 Cr material exhibited improved corrosion resistance in the low-pH/high-temperature environments compared to both N80 and 13 Cr.

The CPP plots in Fig. 20 for the active-passive film behaviour of the 22 Cr material indicates the clear increase in breakdown potentials as the pH of the tested solution decreases (Table 4). Cyclic potentiodynamic polarisation with the 22 Cr duplex steel produced much larger E_{bp} values compared to the 13 Cr stainless steel, signifying that within the

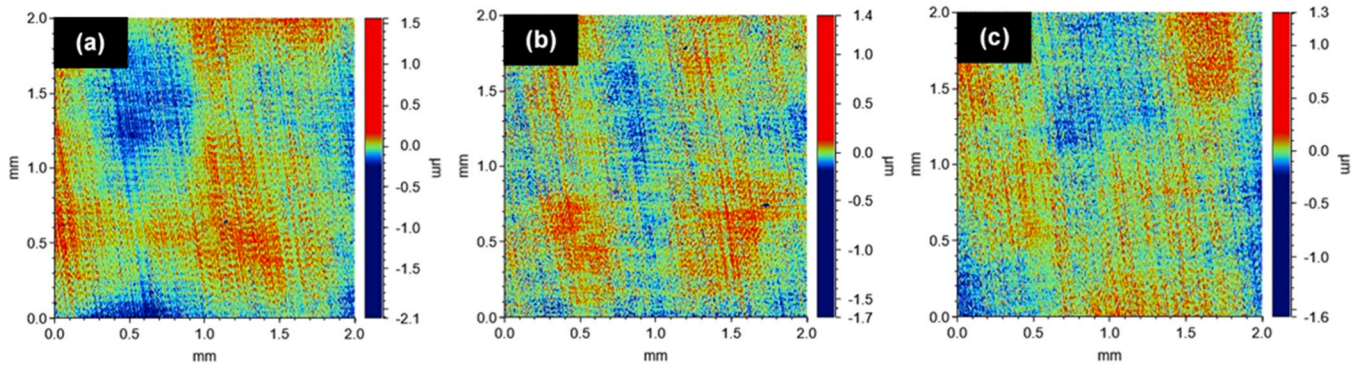

Fig. 21. Surface profiles with corresponding scale bars to indicate localised effects for 2205 duplex stainless steel (UNS S32205) tested at 150 °C with (a) pH 2, (b) pH 3 and (c) pH 4 solutions.

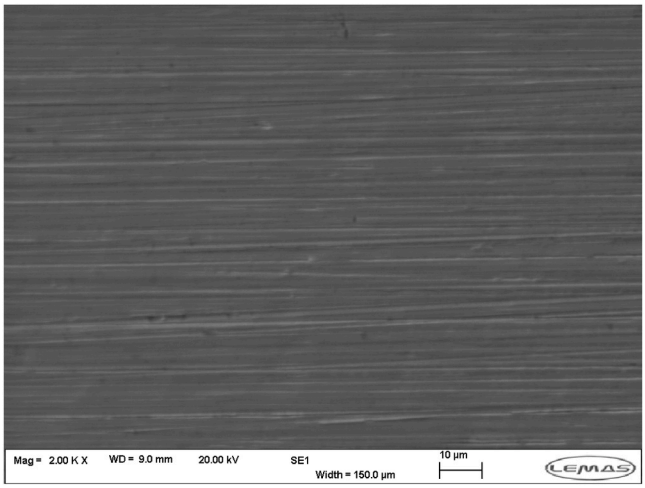

Fig. 22. SEM image of 2205 duplex stainless steel (UNS S32205) from pH 2 and 150 °C test in geothermal brine.

pH 2, 3 and 4 H_2SO_4 environments 22 Cr exhibits superior pitting resistance than 13 Cr. Moreover, the repassivation for 22 Cr within the tested conditions occurs between −0.058 V and −0.086 V, demonstrating that once breakdown of the passive film on the 22 Cr takes place in pH 2, 3 and 4 environments, repassivation of the film occurs a lot more readily than with the 13 Cr material [53].

Surface profiles of the tested 22 Cr duplex steel Fig. 21 shows minimum degradation across pH 2, 3 and 4 solutions with no clear evidence of localised corrosion present on the material.

Microscopy image of the 22 Cr material (Fig. 22) tested in the pH 2 solution at 150 °C did not show any presence of corrosion products on the surface thus confirming minimal material degradation from recorded corrosion rates of 0.09 ± 0.005 mm/year.

Cross-sectioned sample of the 22 Cr material as seen in Fig. 23 also confirmed that the bulk of the stainless steel remained unchanged from the experiment with the expected detection of iron, chromium and oxygen present within the cross-section.

Additionally, Fig. 24 provides a closer view of the cross-sectioned 22 Cr sample with atomic fraction data for the Fe and Cr ions. The initial increase observed from the graph in Fig. 24 is extra data collected from the top of the sample surface containing a thin platinum coating that is prepared ahead of using the FIB. However, as the sample is scanned across the surface and steel interface there is a consistent amount of iron and chromium within the bulk of the material, thus emphasising the minimal degradation identified from the low corrosion rates within the pH 2 H_2SO_4 environment.

4. Conclusions

The capability of the N80 carbon steel, 13 Cr stainless steel and 22 Cr duplex steel materials within elevated temperatures (80 °C, 120 °C and 150 °C) and low-pH (pH 2, 3 and 4) H_2SO_4 environments was investigated with *in-situ* electrochemistry and surface analytical techniques.

- Mass-loss tests assisted with evaluating average corrosion rates and conducting surface analysis to determine material corrosion performance, but additional tests showed that the early test stages needed to be considered, as evolution in the system pH can vary the corrosivity of the solution, thereby emphasising the importance of correlating mass-loss measurements with further data analyses.
- For N80 experiments over the 20 h test period, measured corrosion rates decreased throughout the course of many experiments. This observation was attributed to pH change (consumption of H^+ ions) and consequently electrochemical corrosion measurements collected during the early stages of the experiment were more representative of the true material behaviour in elevated temperatures and low-pH geothermal environments. However, mass loss measurements proved valuable with regards to correlation and validation of the predicted corrosion rates using linear polarisation resistance.
- Initial corrosion rates of N80 carbon steel were understood to differ by around an order of magnitude as the pH of the solutions changed by one unit in the region pH 2–4. High corrosion rates of around 100 mm/year were recorded for N80 exposed to the pH 2 solution at 150 °C.

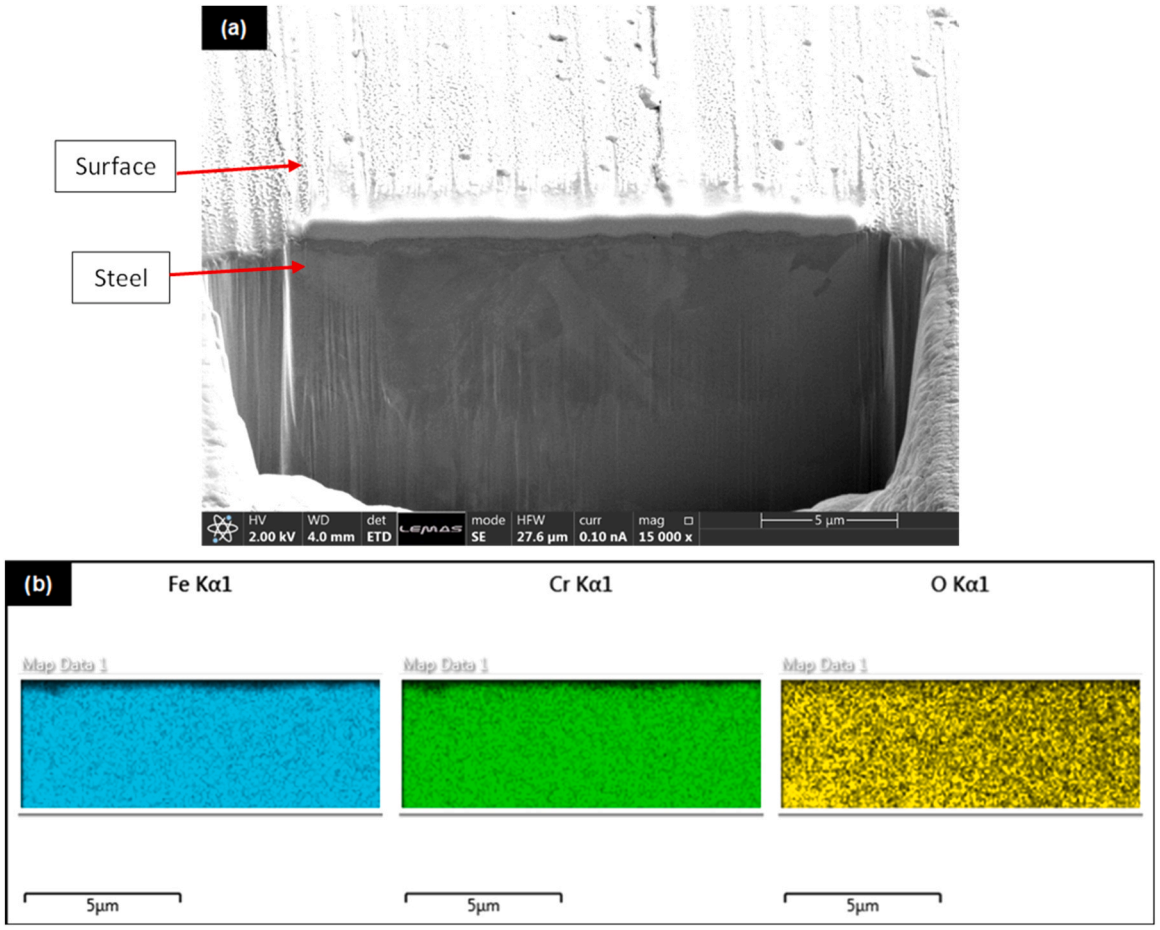

Fig. 23. (a) FIB cross-sectioned 2205 duplex stainless steel (UNS S32205) SEM and (b) EDX image from pH 2 geothermal brine and 150 °C test.

- Examination of the surface layer for the N80 carbon steel tested in H_2SO_4 solution showed no presence of protective $FeSO_4$ layers but instead showed a Fe_3C layer as a result of preferential ferrite dissolution.
- Physical evidence of localised corrosion on the N80 carbon steel showed corrosion depths close to 200 µm with wide and shallow localised regions from being subjected to extreme test conditions (pH 2 and 150 °C). Thus, translating to an average pit growth rate of 87.6 mm/year during the experiment.
- Corrosion rates of 100 mm/year, 10 mm/year and 0.1 mm/year were observed with the N80 carbon steel, 13 Cr stainless steel (UNS S42000) and 22 Cr duplex steel (UNS S32205) respectively within pH 2 solution at 150 °C, hence indicating that with a change of material, corrosion rates varied substantially.
- In pH 3 and pH 4 H_2SO_4 environment 13 Cr stainless steel indicated good pitting resistance, whereas in pH 2 environment 22 Cr duplex steel showed improved pitting resistance and repassivation characteristics from CPP tests.
- No localised corrosion was identified on the 13 Cr (UNS S42000) and 22 Cr (UNS S32205) across the tested geothermal environments within the 20 h timeframe.
- A 40 µm thick, porous, chrome-rich layer was identified on the 13 Cr stainless steel when subjected to the pH 2 solution at 150 °C with an indication of preferential dissolution of iron ions taken place during corrosion. Conversely, 22 Cr duplex steel proved to have superior corrosion resistance in the pH 2 solution at 150 °C with resulting corrosion rates of less than 0.1 mm/year, with a substantially thinner, and more protective layer.
- Future research can explore the corrosion behaviour of materials in ultra-high enthalpy geothermal systems that can exceed operating temperatures of more than 300 °C.

CRediT authorship contribution statement

Joshua Owen: Writing – review & editing, Supervision, Methodology, Formal analysis, Conceptualization. **Kathleen Purnell:** Writing – review & editing, Supervision, Formal analysis. **Joseph Thevakumar:** Writing – review & editing, Writing – original draft, Methodology, Investigation, Formal analysis. **Evgeny Barmatov:** Writing – review & editing, Supervision, Resources, Methodology, Funding acquisition, Formal analysis, Conceptualization. **Richard Barker:** Writing – review & editing, Supervision, Project administration, Methodology, Funding acquisition, Formal analysis, Conceptualization.

Declaration of Competing Interest

The authors declare that they have no known competing financial interests or personal relationships that could have appeared to influence the work reported in this paper.

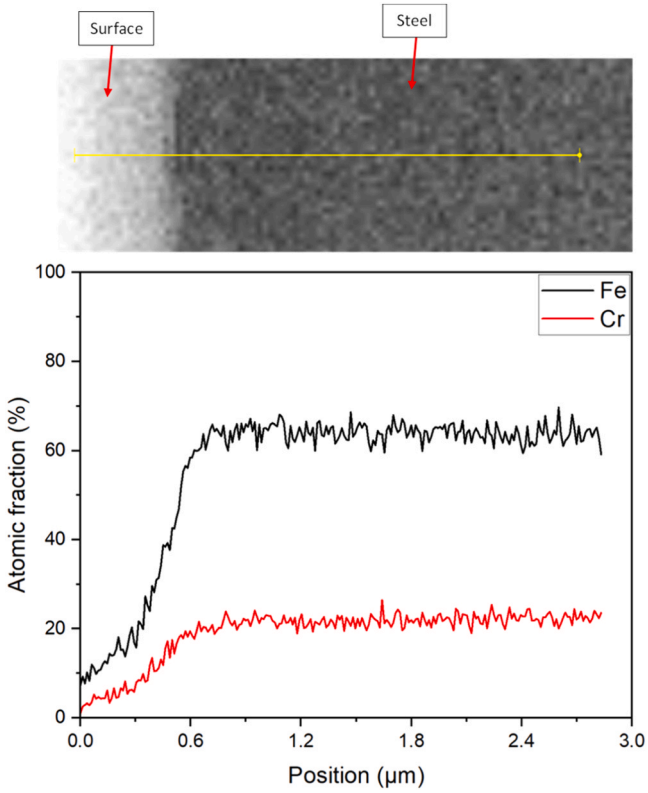

Fig. 24. Graphical data of the 2205 duplex stainless steel (UNS S32205) from pH 2 geothermal brine and 150 °C test showing the amount of iron (Fe) and chromium (Cr) ions present within the material cross-section.

Acknowledgements

The authors would like to show acknowledgement for the funding provided by the Engineering and Physical Sciences Research Council together with SLB. The authors would also like to thank the contributions from Stuart Micklethwaite at University of Leeds Electron Microscopy and Spectroscopy Centre (LEMAS).

Appendix A. Supporting information

Supplementary data associated with this article can be found in the online version at doi:10.1016/j.corsci.2025.113319.

Data availability

Data is being used as part of an ongoing study

References

[1] R. DiPippo, Geothermal power plants: principles, applications, case studies and environmental impact, Butter Heinemann (2012).
[2] W.A. Elders, D. Nielson, P. Schiffman, A. Schriener Jr, Investigating ultra high-enthalpy geothermal systems: a collaborative initiative to promote scientific opportunities, Sci. Drill. 18 (18) (2014) 35–42.
[3] G.O. Fridleifsson, W.A. Elders, S. Thorhallsson, A. Albertsson, The Iceland deep drilling project–A search for unconventional (supercritical) geothermal resources, Proc. World Geotherm. Congr. Antalya Turk. Pap. (2005).
[4] B. Sigfússon, A. Uihlein, 2014 JRC geothermal energy status report, EUR (2015).
[5] S.N. Karlsdottir, K.R. Ragnarsdottir, A. Moller, I.O. Thorbjornsson, A. Einarsson, On-site erosion–corrosion testing in superheated geothermal steam, Geothermics 51 (2014) 170–181.
[6] J. Nogara, S.J. Zarrouk, Evaluation of corrosion resistant alloys as construction material for acidic geothermal wells. Proceedings 36th New Zealand Geothermal Workshop., Auckland, New Zealand, 2014, p. 14.
[7] I.O. Thorbjornsson, G.S. Kaldal, B.C. Krogh, B. Palsson, S.H. Markusson, P. Sigurdsson, A. Einarsson, B.S. Gunnarsson, S.S. Jonsson, Materials investigation of the high temperature IDDP-1 wellhead, Geothermics 87 (2020) 101866.
[8] A.I. Thorhallsson, A. Stefansson, D. Kovalov, S.N. Karlsdottir, Corrosion testing of materials in simulated superheated geothermal environment, Corros. Sci. 168 (2020) 108584.
[9] Bäßler, R., Burkert, A., Saadat, A., Kirchheiner, R. and Finke, M. Evaluation of corrosion resistance of materials for geothermal applications. In: NACE CORROSION: NACE, 2009, pp.NACE-09377.
[10] R. Bäßler, A. Keserovi, J. Sobetzki, H. Sarmiento, Materials evaluation for geothermal applications, energy 3 (2015) 4.
[11] I. Gunnarsson, S. Arnorsson, Silica scaling: the main obstacle in efficient use of high-temperature geothermal fluids. In: International Geothermal Conference, Citeseer, 2003, pp. 30–36.
[12] Lichti, K. Materials selection challenges for geothermal energy projects. In: NACE CORROSION: NACE, 2017, pp.NACE-2017-9258.
[13] Lichti, K. and Wong, J. Corrosion of Ta, Mo, Co, Zr and Ti Alloys in New Zealand geothermal fluids. In: NACE CORROSION: NACE, 2014, pp.NACE-2014-4142.
[14] J. Nogara, S.J. Zarrouk, Corrosion in geothermal environment: part 1: fluids and their impact, Renew. Sustain. Energy Rev. 82 (2018) 1333–1346.
[15] G.L. Rowe Jr, S.L. Brantley, J.F. Fernandez, A. Borgia, The chemical and hydrologic structure of Poás volcano, Costa Rica, J. Volcanol. Geotherm. Res. 64 (3-4) (1995) 233–267.
[16] Y. Taran, E. Kalacheva, Acid sulfate-chloride volcanic waters; formation and potential for monitoring of volcanic activity, J. Volcanol. Geotherm. Res. 405 (2020) 107036.
[17] von Hirtz, P., Kunzman, R., Gallup, D. and Easley, E. New techniques for acid brine corrosion control in geothermal wells.
[18] Perdana, T.S.P., Chen, B.-C., Hackett, L., Robertson-Tait, A. and Thomas, A. Geothermal resource evaluation of the tatun volcano group (TVG) area, Taiwan. In: PROCEEDINGS, 46th Workshop on Geothermal Reservoir Engineering, Stanford University, Stanford, California. 2021, p.13.
[19] S. Arnórsson, A. Stefánsson, J.O. Bjarnason, Fluid-fluid interactions in geothermal systems, Rev. Mineral. Geochem. 65 (1) (2007) 259–312.
[20] I. Krstulović, B. Kulušić, M. Karšulin, The influence of the polarization time on the passivation of iron in sulphuric acid, Corros. Sci. 21 (2) (1981) 95–100.
[21] D. Sazou, M. Pagitsas, C. Georgolios, The influence of chloride ions on the dynamic characteristics observed at the transition between corrosion and passivation states of an iron electrode in sulphuric acid solutions, Electrochim. Acta 37 (11) (1992) 2067–2076.
[22] M. Finster, C. Clark, J. Schroeder, L. Martino, Geothermal produced fluids: characteristics, treatment technologies, and management options, Renew. Sustain. Energy Rev. 50 (2015) 952–966.
[23] K. Nicholson, Geothermal fluids: chemistry and exploration techniques, Springer Science & Business Media, 2012.

[24] M. Keddam, O.R. Mattos, H. Takenouti, Reaction model for iron dissolution studied by electrode impedance: II. Determination of the reaction model, J. Electrochem. Soc. 128 (2) (1981) 266.
[25] M. Keddam, O.R. Mottos, H. Takenouti, Reaction model for iron dissolution studied by electrode impedance: I. Experimental results and reaction model, J. Electrochem. Soc. 128 (2) (1981) 257.
[26] J. Owen, F. Ropital, G.R. Joshi, J. Kittel, R. Barker, Galvanic effects induced by siderite and cementite surface layers on carbon steel in aqueous CO_2 environments, Corros. Sci. 209 (2022) 110762.
[27] Z. Panossian, N.L. de Almeida, R.M.F. de Sousa, G. de Souza Pimenta, L.B. S. Marques, Corrosion of carbon steel pipes and tanks by concentrated sulfuric acid: a review, Corros. Sci. 58 (2012) 1–11.
[28] B. Mazurkiewicz, Anodic passivity of iron in sulphuric acid, Electrochim. Acta 38 (4) (1993) 495–502.
[29] G.H. Damon, Acid corrosion of steel, Ind. Eng. Chem. 33 (1) (1941) 67–69.
[30] I. Epelboin, C. Gabrielli, M. Keddam, J.C. Lestrade, H. Takenouti, Passivation of iron in sulfuric acid medium, J. Electrochem. Soc. 119 (12) (1972) 1632.
[31] M. Keddam, J.F. Lizee, C. Pallotta, H. Takenouti, Electrochemical behavior of passive iron in acid medium: I. Impedance approach, J. Electrochem. Soc. 131 (9) (2016) 1984.
[32] S. Haupt, H.-H. Strehblow, A combined surface analytical and electrochemical study of the formation of passive layers on FeCr alloys in 0.5 m H_2SO_4, Corros. Sci. 37 (1) (1995) 43–54.
[33] C.O.A. Olsson, D. Landolt, Passive films on stainless steels—chemistry, structure and growth, Electrochim. Acta 48 (9) (2003) 1093–1104.
[34] P. Schmutz, D. Landolt, In-situ microgravimetric studies of passive alloys: potential sweep and potential step experiments with Fe–25Cr and Fe–17Cr–33Mo in acid and alkaline solution, Corros. Sci. 41 (11) (1999) 2143–2163.
[35] J. Dobbelaar, E. Herman, J. De Wit, The corrosion behaviour of iron-chromium alloys in 0.5 m sulphuric acid, Corros. Sci. 33 (5) (1992) 765–778.
[36] Y. Yu, S. Shironita, K. Souma, M. Umeda, Effect of chromium content on the corrosion resistance of ferritic stainless steels in sulfuric acid solution, Heliyon 4 (11) (2018).
[37] M. Bojinov, I. Betova, G. Fabricius, T. Laitinen, T. Saario, The stability of the passive state of iron–chromium alloys in sulphuric acid solution, Corros. Sci. 41 (8) (1999) 1557–1584.
[38] E. Huttunen-Saarivirta, E. Isotahdon, Z. Que, M. Lindgren, A. Mardoukhi, J.-B. Jorcin, P. Mocnik, T. Kosec, Y. El Ouazari, S.H. Mameng, Pitting corrosion on highly alloyed stainless steels in dilute sulphuric acid containing sodium chloride, Electrochim. Acta 457 (2023) 142404.
[39] V. Shankar Rao, L.K. Singhal, Corrosion behavior and passive film chemistry of 216L stainless steel in sulphuric acid, J. Mater. Sci. 44 (9) (2009) 2327–2333.
[40] B. Tzaneva, L. Fachikov, R. Raicheff, Pitting corrosion of Cr–Mn–N steel in sulphuric acid media, J. Appl. Electrochem. 36 (3) (2006) 347–353.
[41] K. Ingason, V. Kristjánsson, K. Einarsson, Design and development of the discharge system of IDDP-1, Geothermics 49 (2014) 58–65.
[42] Jacklin, R., Owen, J., Burkle, D., Woollam, R.C. and Barker, R. Characterizing the evolution of iron carbonate in a demanding CO_2 environment using a combined electrochemical impedance spectroscopy and linear polarization resistance approach. In: AMPP Annual Conference + Expo, AMPP-2023-19278, 2023.
[43] Barmatov, E., Hughes, T. and Nagl, M. Performance of organic corrosion inhibitors on carbon steels and high alloys in 4M hydrochloric acid. In: NACE CORROSION: NACE, 2015, pp.NACE-2015-5893.
[44] J.R. Scully, Polarization resistance method for determination of instantaneous corrosion rates, Corrosion 56 (2) (2000) 199–218.
[45] ASTM. ASTM G1-03. Standard Practice for Preparing, Cleaning, and Evaluating Corrosion Test Specimens. 2012.
[46] F. Farelas, B. Brown, S. Nesic, Iron carbide and its influence on the formation of protective iron carbonate in CO_2 corrosion of mild steel, CORROSION 2013 OnePetro (2013).
[47] F. Farelas, M. Galicia, B. Brown, S. Nesic, H. Castaneda, Evolution of dissolution processes at the interface of carbon steel corroding in a CO_2 environment studied by EIS, Corros. Sci. 52 (2) (2010) 509–517.
[48] A. Lazareva, J. Owen, S. Vargas, R. Barker, A. Neville, Investigation of the evolution of an iron carbonate layer and its effect on localized corrosion of X65 carbon steel in CO_2 corrosion environments, Corros. Sci. 192 (2021) 109849.
[49] N. Laycock, R. Newman, Localised dissolution kinetics, salt films and pitting potentials, Corros. Sci. 39 (10-11) (1997) 1771–1790.
[50] T. Rayment, A.J. Davenport, A.J. Dent, J.-P. Tinnes, R.J. Wiltshire, C. Martin, G. Clark, P. Quinn, J.F.W. Mosselmans, Characterisation of salt films on dissolving metal surfaces in artificial corrosion pits via in situ synchrotron X-ray diffraction, Electrochem. Commun. 10 (6) (2008) 855–858.
[51] Y. Hua, R. Jonnalagadda, L. Zhang, A. Neville, R. Barker, Assessment of general and localized corrosion behavior of X65 and 13Cr steels in water-saturated supercritical CO_2 environments with SO_2/O_2, Int. J. Greenh. Gas. Control 64 (2017) 126–136.
[52] B. Stypula, J. Banaś, Passivity of chromium in sulphuric acid solutions, Electrochim. Acta 38 (15) (1993) 2309–2314.
[53] T. Bellezze, G. Giuliani, G. Roventi, Study of stainless steels corrosion in a strong acid mixture. Part 1: cyclic potentiodynamic polarization curves examined by means of an analytical method, Corros. Sci. 130 (2018) 113–125.